International Journal of
Molecular Sciences

MDPI

Article

Possible Steps of the Carboxylation of Ribulose-1,5-biphosphate from Intermediates: 2,3-Enediol versus 1,2-Enol

Roman G. Fedunov [1] and Victor A. Sokolov [2,*]

[1] V.V. Voevodsky Institute of Chemical Kinetics and Combustion/Laboratory of Photochemistry, Institutskaya Str. 3, 630090 Novosibirsk, Russia; fedunov@kinetics.nsc.ru
[2] Institute of Molecular and Cellular Biology/Plant Apomixis Laboratory, Acad. Lavrentiev Ave. 8/2, 630090 Novosibirsk, Russia
* Correspondence: sokolov@mcb.nsc.ru

Abstract: Ribulose 1,5-bisphosphate (RuBP) undergoes enolization to initiate fixation of atmospheric carbon dioxide in the plant carbon cycle. The known model assumes the binding of RuBP to the Rubisco active site with the subsequent formation of 2,3-enediol (2,3,4-trihydroxypent-2-ene-1,5-diyl diphosphate). In the present study, it is assumed that 1,2-enol (2,3,4-trihydroxypent-1-ene-1,5-diyl diphosphate) can be formed in the enolization step to initiate the carboxylation reaction. We have used Kohn–Sham density functional theory on WB97X-D3/Def2-TZVP levels to compare the reaction barriers in the two ways. We considered the pathways of carboxylation of 1/2-ene (mono/di)ol via the C1 and C2 carbons without taking into account the binding of RuBP to the magnesium ion. Calculations of Gibbs free energies confirm the equal probability of the formation of 2,3-enediol and 1,2-enol. Quantum–chemical modeling of enolization and carboxylation reactions supports the important role of the bridging water molecule and diphosphate groups, which provide proton transfer and lower reaction barriers. The results show that carbon dioxide fixation can occur without a magnesium ion, and binding with C1 can have a lower barrier (~12 kcal/mol) than with C2 (~23 kcal/mol).

Keywords: photosynthesis; Rubisco; enolization; carboxylation

Citation: Fedunov, R.G.; Sokolov, V.A. Possible Steps of the Carboxylation of Ribulose-1,5-biphosphate from Intermediates: 2,3-Enediol versus 1,2-Enol. *Int. J. Mol. Sci.* **2021**, *22*, 9749. https://doi.org/10.3390/ijms22189749

Academic Editors: Joanna Grzyb, Beata Myśliwa Kurdziel and Katarzyna Gieczewska

Received: 26 July 2021
Accepted: 6 September 2021
Published: 9 September 2021

1. Introduction

The lifeforms and ecosystems on planet Earth would look completely different in the absence of photosynthesis, which arose around 3 billion years ago. Thanks to its functioning, the atmosphere of the Earth was enriched with oxygen and new means of chemical exchange became possible. When using this element, the efficiency of oxidative exchange reactions reaches 40%, in contrast to 8–10% when using ferrous iron and sulfur. The high energy efficiency of oxygen anabolism has, as a result, become the basis for the organization of complex food chains, in which competition has contributed to the increased sizes of lifeforms. In addition, oxygen is involved in the formation of strong skeletons in animals and lignin in plants, which is a fundamental requirement for the growth and functioning of physically large organisms. In the absence of free O_2 in the atmosphere, the inhabitants of the Earth would be very limited in size, morphologically rather primitive, and could not have mastered the vast expanses of land.

Due to the extraordinary complexity and multilevel hierarchy of the mechanisms of photosynthesis, it remains largely a poorly understood phenomenon, at least in regard to its unusually low efficiency, which greatly limits the productivity of agricultural plants. In part, nature itself has corrected the previously mastered C3 method of carbon fixation and about 20 million years ago "created" a more efficient C4 cycle. However, it exists only in a small number of genera and is very limited, both ecologically and geographically [1]. Among cultivated cereals, C4 fixation of carbon dioxide is carried out in maize and sorghum. The main grain crops—wheat, rye, barley, and rice—use C3 fixation, and as a result are

significantly inferior in terms of yield. To overcome this limitation, research is being carried out across the world to improve the Benson–Bassem–Calvin (BBC) cycle, which is the main way of incorporating CO_2 in organic metabolism [2], and to explore the possibility of replacing it with other fundamentally different variants of carboxylation reactions during the assimilation of carbon dioxide in plants [3–6].

The first step in the carboxylation mechanism of ribulose-1,5-bisphosphate (RuBP) catalyzed by Rubisco in the BBC cycle is the formation of enediolate, which can then attach CO_2 or O_2 molecules. In the case of the attachment of CO_2 to enediolate, an intermediate 6-carbon compound is formed, which is named 3-keto-2-carboxy-D-arabinitol 1,5-bisphosphate (3kCABP). In the literature, one can find a number of works devoted to the modeling of the steps of the carboxylation of RuBP by quantum–chemical methods [7–10], as well as a combination of quantum–chemical and molecular modeling methods [11–14]. When modeling the RuBP enolization reaction, some authors consider the reaction product to be the 2,3-enediol compound [11] or its deprotonated form, 2,3-enediolate [7–14]. In this study, we assume that 1,2-enol or its deprotonated form can be formed during the enolization step. Herein, we use 2,3-enediol and 1,2-enol to abbreviate the names of key intermediates with the following full names: 2,3,4-trihydroxypent-2-ene-1,5-diyl diphosphate and 2,3,4-trihydroxypent-1-ene-1,5-diyl diphosphate. Since the differences between the two are minor, we also use the generic name 1/2-ene(mono/di)ol.

To determine the kinetics, most authors use an enzyme model in which the 2,3-enediolate forms a complex with the magnesium ion Mg^{2+}. In previous studies [7–9,12,13] it was shown that the formation of 3kCABP is energetically favorable; when the 2,3-enediolate interacts with the CO_2 molecule the equilibrium shifts towards the reaction products. Kannappan and Grady point out that Rubisco is a very ineffective enzyme with a low catalytic rate of CO_2 fixation [7]. Therefore, in this study, the steps of enolization and CO_2 fixation are modeled without the magnesium ion. We hope that authors studying the influence of Rubisco on the pathway of the carboxylation reaction may be interested in the mechanisms of enolization and CO_2 fixation when the oxygen atoms of RuBP cannot bind to the magnesium ion.

These modeling features were chosen since in a previously published work [6] we considered the possibility of increasing the efficiency of photosynthesis by changing the enolization pathway of ribulose-1,5-bisphosphate and the attachment of carbon dioxide to the first carbon atom of the RuBP with the formation of 2,6-bisphosphate gluconic acid (BPGA). The carboxylation of RuBP via this pathway immediately leads to the formation of 6-atomic carbohydrates and avoids photorespiration, which theoretically should give at least a 25% increase in plant productivity. Thus, the main objectives of the study are: (1) estimation of the energy barrier for RuBP carboxylation by the first carbon atom; (2) comparison to the barrier of carboxylation in the classical BBC cycle.

2. Results

In order to reveal the preferred pathways for the fixation of carbon dioxide by the 1/2-ene(mono/di)ol molecules, quantum–chemical calculations of the reagents, their key intermediates and probable products were performed. Figure 1 shows the schematic structures of the main compounds under study. Table 1 shows the energy characteristics of the compounds, as well as the charges on the atoms involved in the formation of the double bonds between the carbons of the 1/2-ene(mono/di)ol molecules. Rows 1–3 of the table lists the main reagents: RuBP, including its two protonated forms with an explicit water molecule, $RuBP1^{+}\cdot H_2O$ (a proton attached to a carbonyl oxygen) and $RuBP2^{+}\cdot H_2O$ (a proton attached to one of the phosphate oxygens). The key intermediates are listed in rows 4–7. The characteristics of 1/2-ene(mono/di)olate ions are also calculated, since 2,3-enediolate is traditionally used in many enolization and carboxylation reaction schemes. The possible products of carboxylation are listed in rows 8–11. Since BPGA has an increased number of hydrogen atoms compared to 3kCABP, it is difficult to evaluate the energetically favorable carboxylated form after CO_2 fixation. Therefore, additional quantum–chemical

calculations were performed for CABP, which contains the same number of atoms as BPGA (Appendix A).

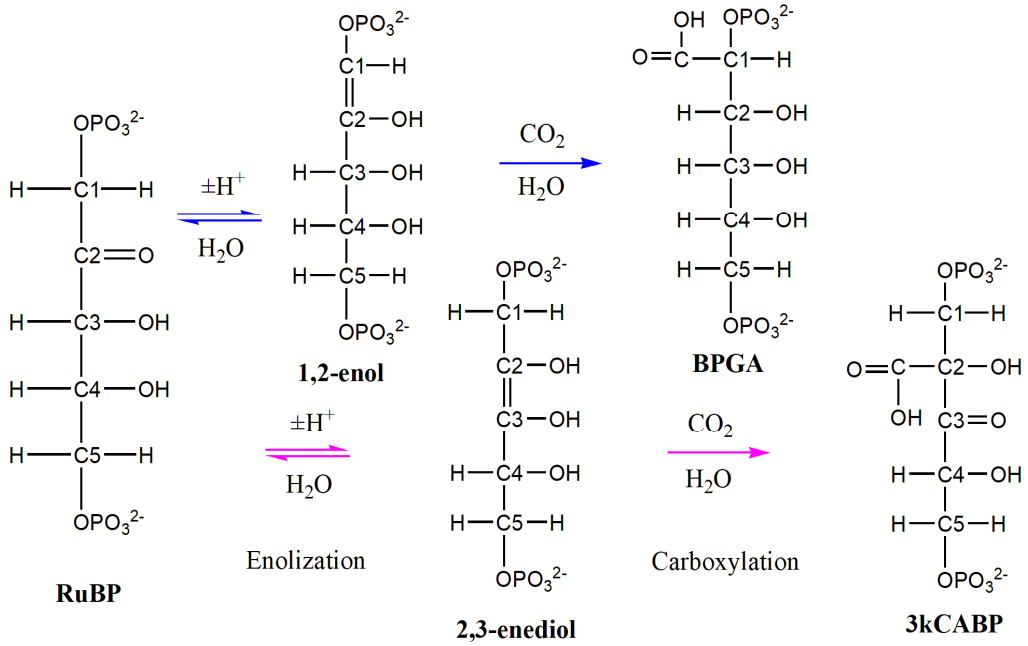

Figure 1. Pathways of enolization and carboxylation reactions via carbon atoms C_1 (blue) and C_2 (purple).

Table 1. Electronic and energy characteristics of the studied molecules. The total charge of the molecule, Q; multiplicity, M; charges on atoms, q_{C1}, q_{C2}, q_{C3}; total energy, E_0 (eV); Gibbs free energy, G_0 (eV); energy of the highest occupied molecular orbital, E_{HOMO} (eV); energy of the lowest unoccupied molecular orbital, E_{LUMO} (eV).

No	Molecule	Q	M	q_{C1}	q_{C2}	q_{C3}	E_0	G_0	E_{HOMO}	E_{LUMO}
1	RuBP	−4	1	−0.105	0.347	−0.052	−46,437.91	−46,434.57	−8.08	1.55
2	$RuBP1^+ \cdot H_2O$	−3	1	−0.025	0.262	0.124	−48,530.12	−48,525.85	−8.27	−0.16
3	$RuBP2^+ \cdot H_2O$	−3	1	−0.040	0.315	0.020	−48,531.77	−48,527.58	−8.31	1.28
4	1,2-enol	−4	1	−0.060	0.073	0.129	−46,437.76	−46,434.44	−7.64	3.43
5	1,2-enolate	−5	1	−0.317	0.177	0.149	−46,424.13	−46,421.11	−6.14	3.88
6	2,3-enediol	−4	1	−0.032	0.106	0.103	−46,437.75	−46,434.39	−7.65	3.32
7	2,3-enediolate	−5	1	0.048	−0.012	0.106	−46,424.27	−46,421.25	−5.97	4.14
8	BPGA	−4	1	0.002	0.068	0.075	−51,603.38	−51,599.04	−6.55	2.20
9	CABP	−4	1	−0.094	0.296	0.006	−51,603.53	−51,599.18	−8.09	2.45
10	3kCABP	−4	1	−0.122	0.254	0.339	−51,570.72	−51,567.08	−8.35	1.24
11	H_2O	0	1	-	-	-	−2080.34	−2080.25	−11.36	3.50
12	H_3O^+	1	1	-	-	-	−2091.54	−2091.10	−15.95	2.38
13	CO_2	0	1	0.474	-	-	−5132.52	−5132.76	−12.80	3.23

The calculated geometric and electronic structures of all compounds included in Table 1 are detailed in Appendix A (Figures A1–A11). The molecules RuBP, 1/2-ene(mono/di)ol, BPGA and CABP have a linear structure. The carbon atoms C_1-C_5 form an extended chain. The distance between the phosphorus of the OPO_3 groups is in the range of 8.5–9.3 Å. The carbon chain of the 3kCABP molecule is more compact, and the molecule is globular in shape. The distance between phosphorus atoms is 7.3 Å.

Analyzing the bond lengths of the molecules shown in Figures A1–A10, we see that strong hydrogen bonds are formed between the hydrogen and oxygen atoms of the hydroxyl groups. The oxygen atoms of the OPO_3 groups are also involved in the formation

of hydrogen bonds. Due to the formation of additional hydrogen bonds, the total energy of the molecule can be slightly reduced. Consequently, the globular structure of molecules is more energetically favorable, which makes it possible to explain the appearance of negative frequencies in the Hessian for some linear molecules. Table 1 shows that the charges on carbon atoms can change significantly due to protonation of the RuBP molecule, deprotonation of 1/2-ene(mono/di)ol, and the transformation of CABP molecule into its 3-keto form.

2.1. Enolization

According to the scheme presented in ref. [11] the conversion of RuBP to 2,3-enediol requires a proton exchange between carbon C_3 and the carbonyl group. The authors consider that the enzyme catalyzes enolization with a specific active-site residue, which acts as a base that removes protons from the C_3 atom, and afterward an acid protonates the carbonyl oxygen. We suppose that the bonding of the proton with the carbonyl oxygen RuBP can contribute to the proton detachment from the C_3 carbon, since the charge on the C_3 atom becomes positive (Figure A2). A decrease in the C_1–C_2 and C_2–C_3 bond lengths in $RuBP1^+$ can lead to protonated 1/2-ene(mono/di)ol with C_1=C_2 or C_2=C_3 double bonds.

The protonated form: $RuBP2^+$ (Figure A3) is obtained by calculating $RuBP1^+$ when the proton is oriented towards the OPO_3 group. Geometrical optimization unexpectedly results in proton transfer from the carbonyl oxygen to the nearest oxygen of the OPO_3 group. Indeed, $RuBP2^+$ has a lower total energy than $RuBP1^+$ and the difference is significant, at 1.65 eV. However, no decrease in the lengths of the C_1–C_2 and C_2–C_3 bonds is observed. The electronegativity of C_1 and C_3 atoms decreases, but not as much as upon protonation of carbonyl oxygen in $RuBP1^+$.

To estimate the probability of proton detachment from C_1 and C_3 atoms, let us calculate the relaxed surface scans of the total energies along the reaction coordinates $R_{C(1)\text{-}H}$ and $R_{C(3)\text{-}H}$. Both protonated forms $RuBP1^+$ and $RuBP2^+$ are complemented by a single water molecule (Figures A2 and A3), which can act as a proton acceptor and a bridge to the transport of protons from carbon C_1 or C_3 to the oxygen of the OPO_3 group. In each model reaction, the C-H bond length sequentially increases by 0.1 A. The reaction coordinate has a fixed value, while all other geometric parameters are optimized to calculate the dependence of the total energy on the reaction coordinate. Figure 2 shows the total energies of model reactions with respect to the total energy, E_0, of the initial configurations presented in Figures A2 and A3.

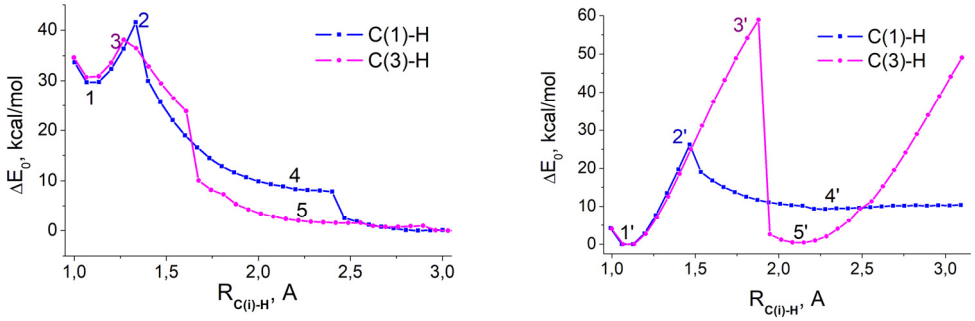

Figure 2. The energy relaxed surface scans of proton detachment from C_1 (blue) and C_3 (purple) carbons in: (**a**) $RuBP1^+ \cdot H_2O$; E_0 = −48,530.12 eV (−1,119,104.57 kcal/mol). (**b**) $RuBP2^+ \cdot H_2O$; E_0 = −48,531.77 eV (−1,119,142.62 kcal/mol).

To remove a proton from carbon atoms C_1 or C_3, it is necessary to overcome a barrier of about 45 kcal/mol (Figure 2a). Acting as a bridge, the water molecule can accept the detached proton, while the water proton is transferred to the oxygen of the OPO_3 group, resulting in the formation of the protonated 1,2-enol$^+$ (states 4 and 4′ in Figure 3)

or 2,3-enediol$^+$ (state 5 in Figure 3). These pathways are represented in Figure 3 by transformations $1 \rightarrow 2 \rightarrow 4$, $1 \rightarrow 3 \rightarrow 5$ and $1' \rightarrow 2' \rightarrow 4'$. In the case of $1' \rightarrow 3' \rightarrow 5'$, the proton detached from carbon C_3 is transferred to carbon C_2, which does not lead to the protonated form of 1/2-ene(mono/di)ol. It should be noted for the $1' \rightarrow 2' \rightarrow 4'$ pathway, that the proton of the $OPO_3{}^{-1}H$ group can be transferred to the carbonyl oxygen, while the proton of water is transferred to the opposite OPO_3 group.

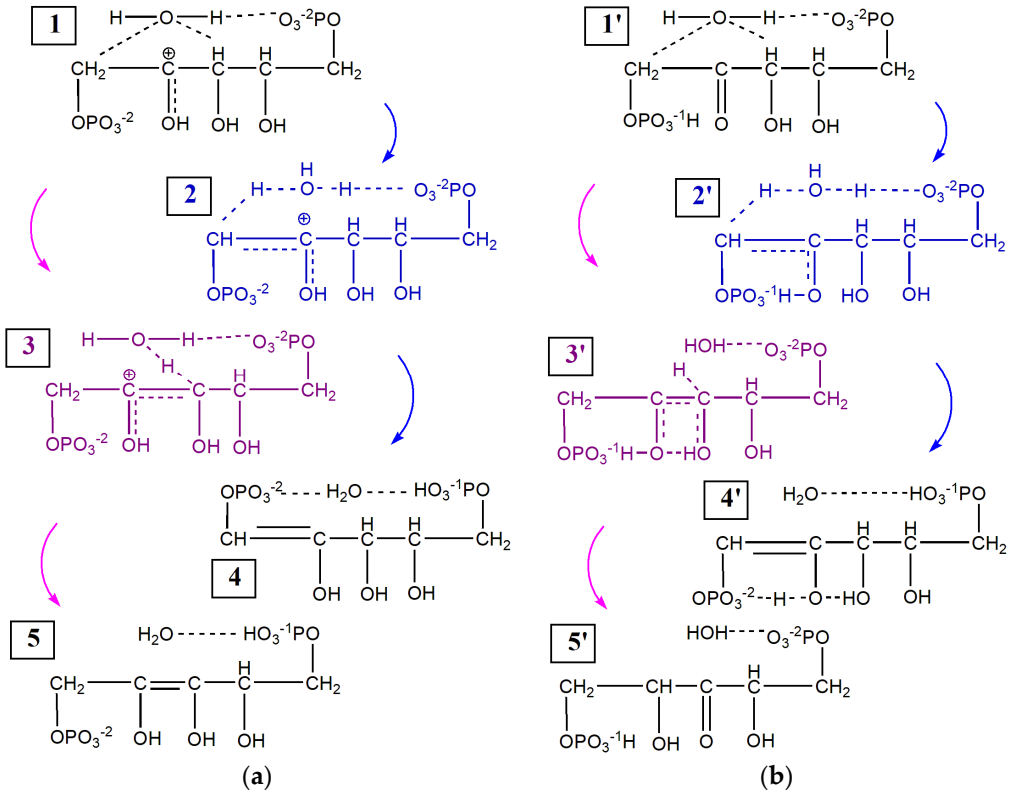

Figure 3. The scheme of enolization via proton detachment from C_1 (blue) and C_3 (purple) carbons in: (**a**) RuBP1$^+$·H_2O; (**b**) RuBP2$^+$·H_2O. The initial states are (1) and (1′). The states corresponding to the top of the barrier (2), (3) and (2′), (3′) are colored. The products of enolization are as follows: (Z)-5-(hydrogen phosphonatooxy)-2,3,4-trihydroxypent-1-enyl phosphate—states (4) and (4′), (Z)-5-(hydrogen phosphonatooxy)-2,3,4-trihydroxypent-2-enyl phosphate—tate (5). The product of tauto-merization is 5-(hydrogen phosphonatooxy)-2,4-dihydroxy-3-oxopentyl phosphate— state (5′).

Figure 3a shows that the initial state (1), RuBP1$^+$·H_2O, has a higher energy than the configurations of products (4) and (5). In this case, in order to remove a proton from carbon C_1 or C_3, it is necessary to overcome the barrier of 8–11 kcal/mol. However, to obtain an advantageous initial configuration, approximately an additional 30 kcal/mol of energy is required. Provided that protons can easily attach and detach from OPO_3 groups, we can assume that both reaction pathways lead to the equally likely formation of both 1,2-enol$^+$ and 2,3-enediol$^+$.

In the case of the initial state (1′), RuBP2$^+$·H_2O, only one pathway $1' \rightarrow 2' \rightarrow 4'$ leads to the formation of protonated 1,2-enol$^+$ (4′). The barrier is 28 kcal/mol (Figure 2b), which is much less than the 48 kcal/mol observed for the $1 \rightarrow 2 \rightarrow 4$ transformations (Figure 2a). To provide the tautomerization pathway, $1' \rightarrow 3' \rightarrow 5'$, it is necessary to overcome the 60 kcal/mol barrier and to reach a distance, $R_{C(3)\text{-}H} \sim 2$ Å, whereas enolization occurs at distances not exceeding 1.5 Å.

2.2. CO_2 Fixation

Since the typical carboxylation reaction models are based on the interaction of CO_2 with 2,3-enediolate [7–14], let us compare the activities of 1,2-enol and 1,2-enolate with 2,3-enediol and 2,3-enediolate, respectively. The activities of the molecules 1/2-ene(mono/di)ol and 1/2-ene(mono/di)olate can be estimated from the quantum–chemical analysis of the charges on the C_1-C_3 carbon atoms and the electronic structure of the boundary molecular orbitals (rows 4–7 in Table 1).

The electronic and geometric structures of 1/2-ene(mono/di)ol molecules are shown in Figures A4 and A6, and their deprotonated forms are shown in Figures A5 and A7. In the case of 1,2-enol, deprotonation of the OH group attached to the C_1 carbon leads to an increase in the negative charge q_{C1} by a factor of 6 (rows 4, 5 in Table 1). In the case of 2,3-enediol, deprotonation of the OH group attached to the C_2 carbon causes a change in the sign of the charge $q_{C(2)}$ from positive to negative (rows 6, 7 in Table 1). An increase in the electronegativity of active centers promotes their interaction with the positively charged carbon atom of the CO_2 molecule. In addition, the deprotonation of 1/2-ene(mono/di)ol leads to a slight lengthening of the double bond between carbon atoms: C_1=C_2 increases by 0.026 Å in 1,2-enolate and C_2=C_3 increases by 0.033 Å in 2,3-enediolate.

The 1/2-ene(mono/di)ol molecules have insignificant differences in electronic structure, which is expressed in the similar values of the electronic charges on the C_1-C_5 carbon atoms and close values of the total energies and energies of the boundary molecular orbitals (rows 4 and 6 in Table 1). The main contribution to HOMO of 1,2-enol is made by the following AOs: $p_x(C_1) = 0.17$, $p_x(C_2) = 0.19$, $p_z(C_1) = 0.02$, $p_z(C_2) = 0.02$. The main contribution to the HOMO of 2,3-enediol is made by the following AOs: $p_z(C_2) = 0.11$, $p_z(C_3) = 0.10$, $p_y(C_2) = 0.09$, $p_y(C_3) = 0.09$. In each case, the main contribution is made by the π-orbitals participating in the formation of the double bond.

After deprotonation of the 1/2-ene(mono/di)ol molecules, the main contributions of AOs to HOMO undergo several significant changes. The AO contribution of C_1 carbon to the HOMO of 1,2-enolate becomes dominant: $p_x(C_1) = 0.29$, $p_x(C_2) = 0.08$, $p_z(C_1) = 0.01$, $p_z(C_2) = 0.02$, while the AO contribution of C_2 carbon to HOMO predominates in 2,3-enediolate: $p_z(C_2) = 0.17$, $p_z(C_3) = 0.06$, $p_y(C_2) = 0.1$, $p_y(C_3) = 0.04$. Electrophilic interaction is preferably with the C_1 atom in the 1,2-enolate and with the C_2 atom in the 2,3-enediolate. The HOMO energy of 1,2-enediolate becomes 0.14 eV lower than the HOMO energy of 2,3-enediolate. Thus, the interaction energy between the electrophilic agent (CO_2) and 2,3-enediolate are lower than those of 1,2-enolate, which makes it possible to provide a better affinity for carbon dioxide and to obtain an energetically more favorable product of the carboxylation reaction.

Carboxylation via carbon C_1 leads to the formation of the product 2,6-bisphosphogluconic acid (BPGA, Figure A8) during the reaction of 1,2-enol(ate) with carbon dioxide according to the scheme shown in Figure 1 (blue pathway). In the classic scheme, 2,3-enediol(ate) reacts with carbon dioxide via carbon C_2 as shown in Figure 1 (purple pathway), resulting in the well-known 3-keto-2-carboxy-D-arabinitol -1,5-bisphosphate (3kCABP, Figure A10). Further, the 3-keto compound decomposes at the C_2–C_3 bond into two 3-phosphoglycerate molecules. BPGA decomposition requires further study to explain its incorporation into the metabolic pathway.

To compare the energy characteristics of the carboxylation products for both reaction schemes, the 2-carboxy-D-arabinitol 1,5-bisphosphate (CABP, Figure A9) are calculated. CABP contains the same number of hydrogen atoms as BPGA. Calculations show that the formation of CABP or its 3-keto form is energetically more favorable than the formation of BPGA. The difference in total energies is 0.15 eV, and the difference in Gibbs free energy is 0.14 eV (3.2 kcal/mol). This result shows that 3kCABP is thermodynamically more likely than BPGA. On the other hand, 3kCABP can be quite stable, which can make it difficult to decompose into two 3-phosphoglycerate molecules. Indeed, early attempts to simulate scission of the C_2–C_3 bond demonstrate that the energies of the final products can be higher than the energy of intermediate reagents [7,13].

Using the enolization products of 1,2-enol^{+}·H_2O (state 4′) and 2,3-enediol^{+}·H_2O (state 5) together with carbon dioxide as the initial states (Figures A12 and A13), we calculate the relaxed surface scans along the reaction coordinates $R_{C(1)-C}$ and $R_{C(2)-C}$. In each model reaction, the length of the C_i–C bond between 1/2 carbons of the protonated 1/2-ene(mono/di)ol and carbon of CO_2 is consequently decreased by 0.1 Å. The reaction coordinate has a fixed value, and all other geometric parameters are optimized to calculate the dependence of the total energy on the reaction coordinate. Figure 4 shows the difference between the total energies calculated for each value of the reaction coordinate with respect to the total energy of the final configuration having the lowest energy, E_f. Figure 5 shows two carboxylation schemes via carbon atoms C_1 (blue pathway) and C_2 (purple pathway).

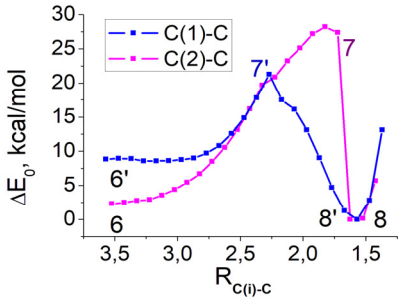

Figure 4. The energy relaxed surface scans of carboxilation via C_1 (blue) and C_2 (purple) carbons, E_f = −53,664.65 eV (−1,237,534 kcal/mol).

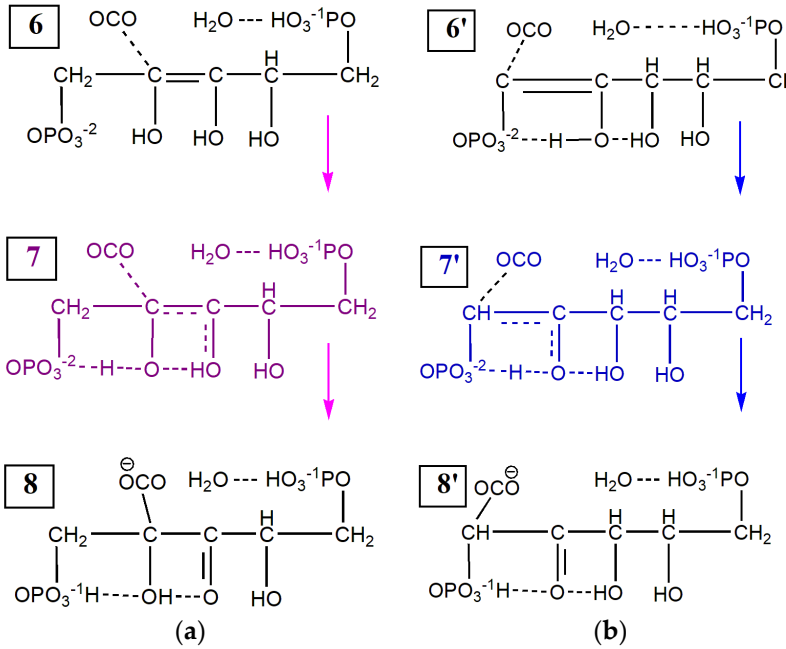

Figure 5. The scheme of carboxylation via C_1 (blue) and C_2 (purple) carbons in: (**a**) 1,2-enol^{+}·H_2O; (**b**) 2,3-enediol^{+}·H_2O. The initial states (6) and (6′) are preliminarily calculated at the stages of enolization. Their optimized geometric structures are shown in Figures A12 and A13, respectively. The states corresponding to the top of the barrier (7) and (7′) are colored. The products of carboxylation are as follows: 5-(hydrogen phosphonatooxy)-2-((hydrogen phosphonatooxy)methyl)-2,4-dihydroxy-3-oxopentanoate—the state (8) excluding water and 2,6-bis(hydrogen phosphonatooxy)-4,5-dihydroxy-3-oxohexanoate—the state (8′) excluding water.

Both the C_1 and C_2 pathways of CO_2 fixation make it possible to obtain a six-carbon compound. Proton transfer between the hydroxyl groups and the oxygen of the OPO_3^{-2} group plays a crucial role in the fixation of CO_2 and the formation of C_2=O or C_3=O

double bonds. The initial state 6′ has a higher total energy value than state 6 because fewer hydrogen bonds are formed here (compare Figures A12 and A13). When state 6 is considered as the initial one, the attachment of CO_2 to the C_2 atom and further the formation of the C_3=O double bond requires the larger consumption of energy due to the simultaneous transfer of two protons, as well as the greater destruction of hydrogen bonds. Thus, the energy barrier of CO_2 binding to carbon C_1 (13 kcal/mol) is lower than to carbon C_2 (27 kcal/mol).

3. Discussion

The quantum–chemical modeling of enolization and carboxylation reactions performed in this work differs from the reaction pathways presented in Figure 1. The main difference lies in the choice of active forms of reagents and intermediate compounds that we use to calculate the reaction barriers and assess the energy properties of the compounds used in the literature. To compare both approaches, it is possible to estimate the thermodynamic properties of the reagents and products included in Figure 1, based on the results of calculating the Gibbs free energy.

Let us compare the Gibbs free energies of RuBP$(1/2)^+ \cdot H_2O$ and RuBP together with H_3O^+ combined into a common system:

$$G_0(\text{RuBP} + H_3O^+) = -48{,}525.67 \text{ eV}. \quad (1)$$

The Gibbs free energy in Equation (1) is calculated as the summary energy of the molecules in brackets. A minor difference (0.18 eV) is observed between the energy of RuBP$1^+ \cdot H_2O$ and the sum of the energies of its constituents, which should be a consequence of a decrease in the Gibbs free energy of RuBP$1^+ \cdot H_2O$ due to the formation of additional hydrogen bonds. On the other hand, a larger difference (1.91 eV) is observed for RuBP$2^+ \cdot H_2O$, which points to the advantage of direct protonation of the RuBP diphosphate oxygen.

The next step is to compare the energies of isolated molecules and bound systems participating in the fixation of CO_2 as intermediate states. We calculate the Gibbs free energy, $G_0(1/2)$, of the system including 1/2-ene(mono/di)ol (Figure 1) along with CO_2 and H_3O^+ to compare them with $G_0(6'/6)$ of the systems being the initial states in the model reaction of the carboxylation (Figures A12 and A13):

$$G_0(1) = -53{,}658.50 \text{ eV}. \; G_0(6') = -53{,}659.65 \text{ eV}. \quad (2)$$

$$G_0(2) = -53{,}658.25 \text{ eV}. \; G_0(6) = -53{,}659.83 \text{ eV}. \quad (3)$$

The difference between $G_0(1/2)$ and $G_0(6'/6)$ is about 1.5 eV, which corresponds to the first result observed for RuBP$2^+ \cdot H_2O$. This confirms the high probability of the reaction with protonated diphosphate oxygen.

Finally, we compare the products shown in Figure 1, adding simple molecules, with the products obtained in the model reaction to equalize them in terms of the number of hydrogen and oxygen atoms. Applying the alignment procedure to the products obtained via pathway C_1, we calculate the Gibbs free energies:

$$G_0(\text{BPGA} + H_3O^+) = -53{,}690.14 \text{ eV}. \; G_0\left(8' + H_2O - \frac{1}{2}O_2\right) = -53{,}699.01 \text{ eV}. \quad (4)$$

To align the oxygen atoms in the left and right parts of Equation (4), the one oxygen should be excluded from the right part. The Gibbs free energy in the left part is the summary energy of the molecules in brackets. To compare the Gibbs free energies of both products, the sum of the energies of the state (8′) and H_2O in the right part are reduced by half $^3O_2$ energy, as indicated in the caption to Figure A10d.

Applying the alignment procedure to the products obtained via the C_2 pathway, we calculate the Gibbs free energies:

$$G_0(3kCABP + H_3O^+) = -53{,}658.18 \text{ eV}. G_0(8) = -53{,}664.55 \text{ eV}. \quad (5)$$

The Gibbs free energy in the left part is the summary energy of molecules in brackets. Although the BPGA and 3kCABP compounds in the left parts of Equations (4) and (5) are considered as final products, their energies are higher than those in the right parts. Both pathways give differences of the order of 6–9 eV between the products shown in Figure 1 and the products having the minimum of curves in Figure 5. Since two protons are attached to both phosphate groups, the Gibbs free energies of the structures (8/8′) are greatly reduced. The formation of multiple hydrogen bonds in these model systems can also reduce energy.

Calculations of the Gibbs free energies of intermediate compounds and products make it possible to compare their concentrations for each pathway of carboxylation. We consider that the concentrations of 1,2-enol and 2,3-enediol can be in equilibrium, since their Gibbs free energies differ insignificantly. This difference can be compensated for by the reconfiguration of molecules and the rearrangement of hydrogen bonds in the course of thermal fluctuations. Taking into account the lower reaction barrier via the C_1 pathway and the same Gibbs free energies for (8/8′) systems, we believe that the CO_2 binding to the C_1 atom is more likely.

Quantum–chemical calculations of the energy barriers of the proton detachment from carbon C_1 or C_3 show that modeling can be successfully carried out for a protonated RuBP molecule (Figure 3). In this case it is possible to calculate the reaction barrier considering only one reaction coordinate; however, the exchange of protons usually occurs simultaneously, so a more correct simulation is to calculate the relaxed surface scan, which includes two or more reaction coordinates. So the reaction barriers for some pathways can be significantly lower, and the disruption observed for the stage $3' \rightarrow 5'$ in Figure 3b can be avoided. However, we are convinced that the enolization barriers calculated using the same procedures and conditions for both C_1 and C_3 pathways are an acceptable means for comparing the probabilities of 1/2-ene(mono/di)ol$^+$ formation.

The additional proton in the RuBP system explains the important role of OPO_3 groups; the proton has the advantage of attaching to one of the oxygen atoms of the diphosphate groups. A similar result was found in ref. [9], obtained by the authors in the course of modeling the reaction of carboxylation—the intermediate (Figure 1 in ref. [9]) contains the OPO_3H^- group. In our work, it is shown that the proton detachment from carbon C_1 or C_3 can be accompanied by protonation of the OPO_3 group. CO_2 binding also promotes proton transfer to the OPO_3 group. Thus, at least two protons are needed to proceed the carboxylation reaction. The first proton activates RuBP to then produce the intermediate 1/2-ene(mono/di)ol$^+$. The transfer of the second proton to another OPO_3 group facilitates the attachment of CO_2.

We understand that the fixation of carbon dioxide in plants is a complex process in which many compounds are involved, in addition to the Rubisco enzyme having magnesium ions (Mg^{2+}) which provide enzymatic activity. Typically, modeling involves many auxiliary compounds in order to initiate a proton migration and to provide a convenient configuration of RuBP with Mg. A water molecule coordinated with Mg is a bridge between CO_2 and Mg [7,13,14], an unprotonated HIS24 residue is able to remove the O3 proton from RuBP [13], a GLU60 with an accepted proton is an initiator for the formation of Grotthuss chains. They play a special role in the mechanisms of the enolization and carboxylation reactions [9].

To evaluate the effect of the magnesium ion from the opposite point of view, we use a simple model without Mg^{2+} and auxiliary compounds, except for the water bridge. Activated RuBPs with two different protonated sites—O2 and OPO_3 are used as the initial states of enolization. The formation of 1,2-enol with a protonated OPO_3 group occurs only along the C_1 pathway, overcoming the minimum barrier of 28 kcal/mol. Since the oxygen

atoms O2 and O3 are not bonded to Mg, the C_3 pathway leads to the transfer of a proton from O3 to O2 without the formation of protonated 2,3-enediol. Probably, the interaction of both oxygen atoms with Mg can help to avoid proton transfer between them in RuBP and reduce the barrier of the enolization stage.

Using protonated 1,2-enol, we show that binding of CO_2 to C_1 can overcome the barrier of 10–20 kcal/mol. The experimentally observed barriers for the enolization and carboxylation stages are about 15 kcal/mol [9]. Theoretical research carried out in ref. [9] demonstrated good agreement between the calculated and experimental energies of enolization and carboxylation using the Kohn–Sham density functional theory at the B3LYP/6-31G* and B3LYPgCP-D3 levels. This prompted us to choose the WB97X-D3 functional, which are efficient DFT-D3 corrected variants.

Modeling the binding of CO_2 to C_2 without taking into account the interaction with Mg shows that the formation of a six-carbon compound is possible with the simultaneous transfer of a proton from O2 to OPO_3 and from O3 to O2. The barrier in this case is about 25 kcal/mol. However, the interaction of O2 and O3 with the magnesium ion may not require proton transfer from O3 to O2. The reaction can proceed in a classical way.

To clarify the probabilities of these processes, additional studies on carboxylation are required, taking into account Mg and auxiliary compounds, as well as two enolization pathways via the C_1 and C_3 atoms. On the other hand, we hope that the study of the mechanisms of enolization and carboxylation presented in this work will help studies of artificial systems for fixing carbon dioxide without the active influence of Rubisco components.

The presented theoretical study is only the first step towards understanding the phenomenon of carboxylation with the participation of 1,2-enol. While this allows probabilistic estimates to be made, experimental studies are undoubtedly required to test this hypothesis.

4. Materials and Methods

Quantum–chemical calculations were carried out using the restricted Kohn–Sham DFT process with the WB97X-D3 [15–17] functional and the RIJCOSX [18] approximation. The wave function was calculated using the def2-TZVP [19,20] basis set, while the self-consistency procedure was performed using the TightSCF criterion. The DFT grid was set to GRID5 for all def2-TZVP calculations. Before optimization, the initial shape of all biomolecules was set to linear. The convergence criterion for geometry optimization was chosen as TIGHTOPT. No symmetry restrictions were applied in the calculations. The geometric and electronic properties of the optimized structures were obtained using LR-CPCM [21–23] to account for the implicit water solvent, and in some cases a single water molecule was added explicitly. The Hessian was calculated to test negative frequencies. The relaxed surface scan was performed to calculate the reaction barriers. The ORCA 4.2.1 [24] software package was used for all calculations. ChemCraft [25] software was used for the visualization of geometric structures.

Author Contributions: Conceptualization, V.A.S.; methodology, R.G.F.; validation, V.A.S.; formal analysis, R.G.F.; investigation, V.A.S. and R.G.F.; writing—original draft preparation, V.A.S. and R.G.F.; writing—review and editing, V.A.S. and R.G.F.; visualization, R.G.F.; supervision, V.A.S.; project administration, V.A.S.; funding acquisition, V.A.S. All authors have read and agreed to the published version of the manuscript.

Funding: This research received no external funding.

Institutional Review Board Statement: Not applicable.

Informed Consent Statement: Not applicable.

Data Availability Statement: https://www.researchgate.net/publication/354271173_Results_of_calculation.

Acknowledgments: The authors are deeply grateful to Carly Schramm for extensive revision of our English text, which has undoubtedly led to this work becoming more understandable.

Conflicts of Interest: The authors declare no conflict of interest.

Appendix A

Figures A1–A11 in Appendix A show the optimized geometric structures of the compounds listed in Table 1. Bond lengths are indicated between atoms and Mulliken charges are indicated on the atoms. The total charge, Q; multiplicity, M; total energy, E_0 and Gibbs free energy, G_0 of each molecule are presented in the figure caption.

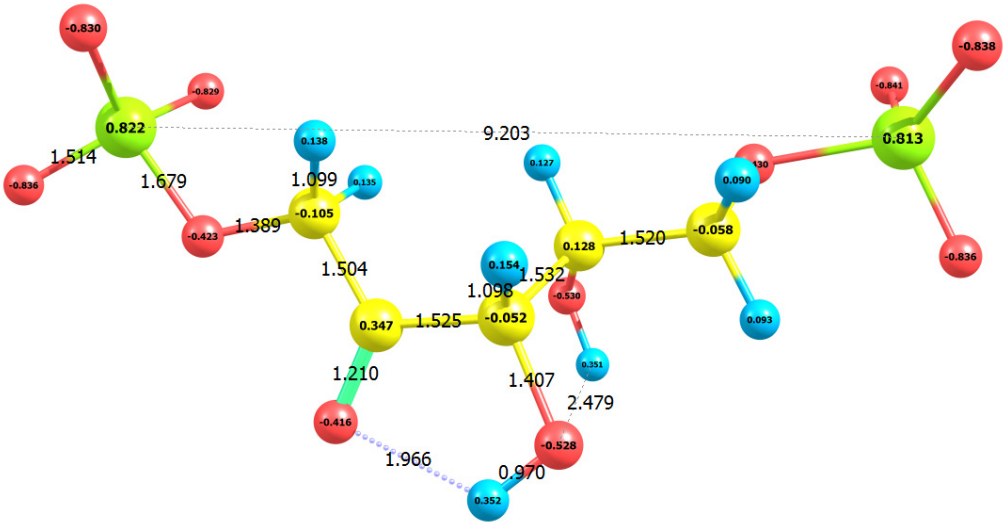

(**a**)

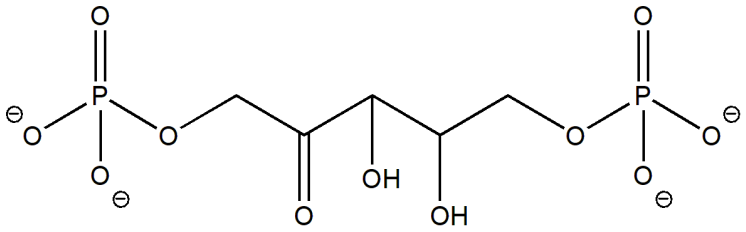

(**b**)

Figure A1. (**a**) The calculated geometric and electronic structure of ribulose-1,5-bisphosphate (RuBP); Q = −4, M = 1, E_0 = −46,437.91 eV, G_0 = −46,434.57 eV. Hessian has negative frequencies: −31.54, −7.59 (cm^{-1}). (**b**) The scheme of 2,3-dihydroxy-4-oxopentane-1,5-diyl diphosphate.

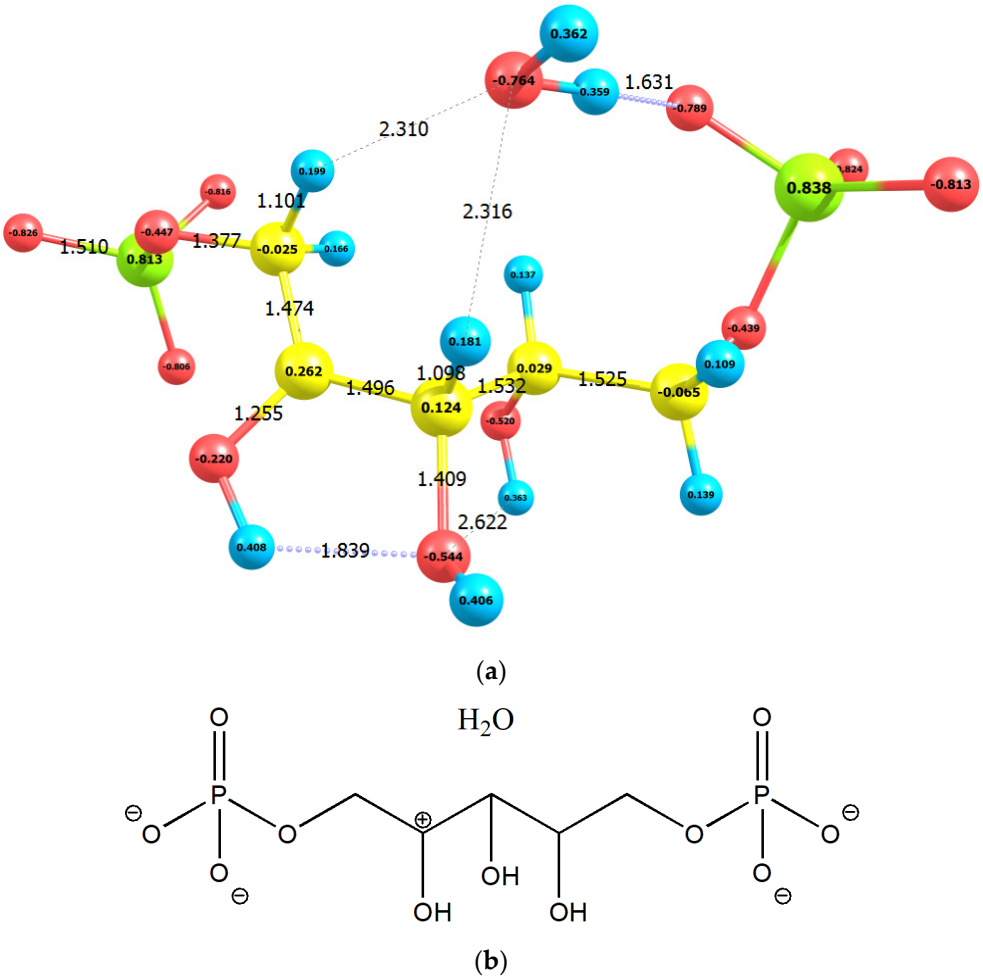

Figure A2. (**a**) The calculated geometric and electronic structure of protonated ribulose-1,5-bisphosphate with single water molecule ($RuBP1^{+}{\cdot}H_2O$); Q = −3, M = 1, E_0 = −48,530.12 eV, G_0 = −48,525.85 eV. Hessian has negative frequencies: −26.56 (cm^{-1}). (**b**) The scheme of 2,3,4-trihydroxypentan-2-ylium-1,5-diyl diphosphate.

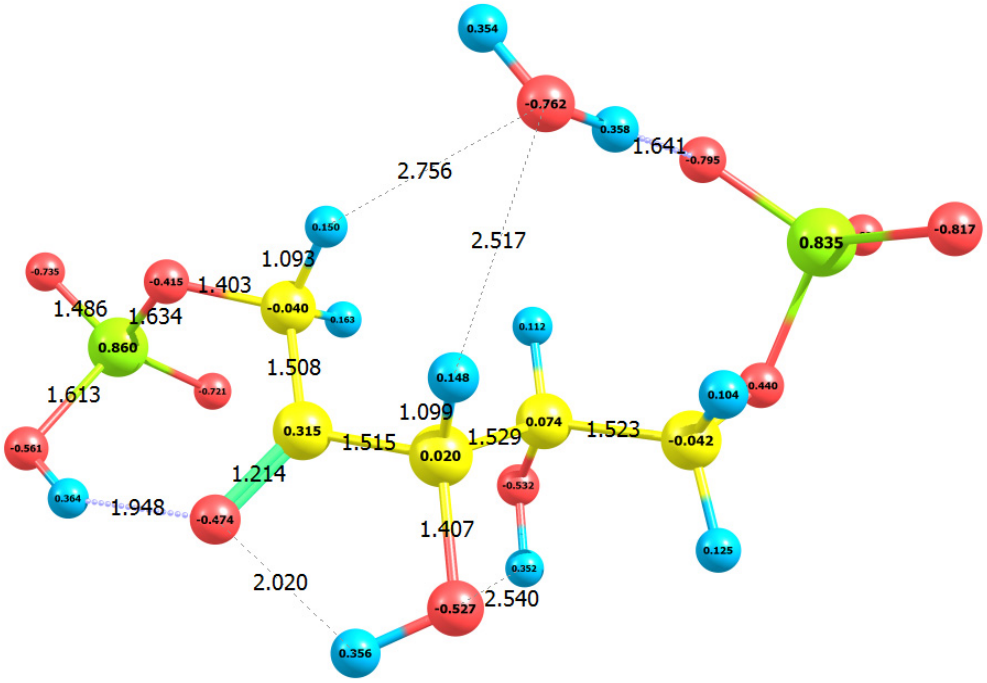

(**a**)

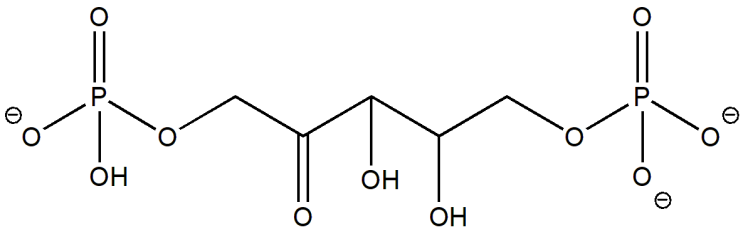

(**b**)

Figure A3. (**a**) The calculated geometric and electronic structure of protonated ribulose-1,5-bisphosphate with single water molecule ($RuBP2^{+}\cdot H_2O$); Q = −3, M = 1, E_0 = −48,531.77 eV, G_0 = −48,527.58 eV. Hessian has no negative frequencies. (**b**) The scheme of 5-(hydrogen phosphonatooxy)-2,3-dihydroxy-4-oxopentyl phosphate.

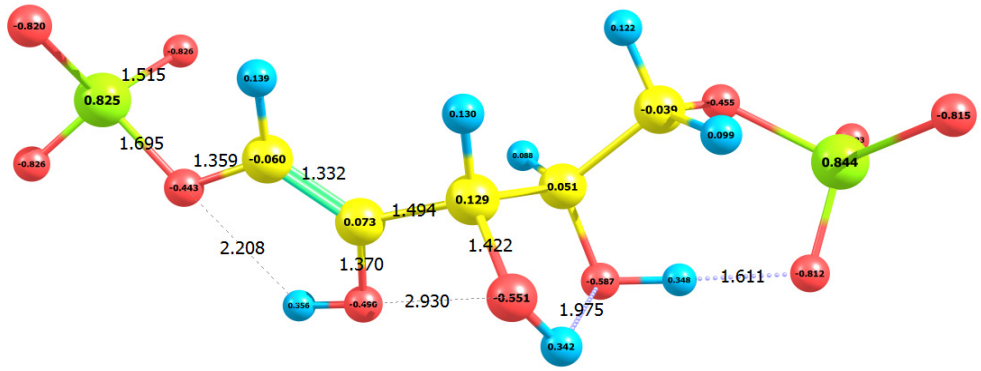

(**a**)

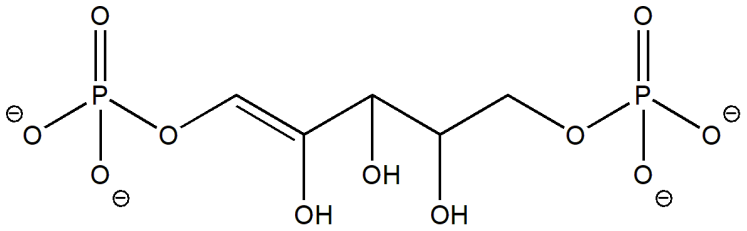

(**b**)

Figure A4. (**a**) The calculated geometric and electronic structure of 1/2-ene(mono/di)ol (1,2-enol); Q = −4, M = 1, E_0 = −46,437.76 eV, G_0 = −46,434.44 eV. Hessian has no negative frequencies. (**b**) The scheme of (Z)-2,3,4-trihydroxypent-1-ene-1,5-diyl diphosphate.

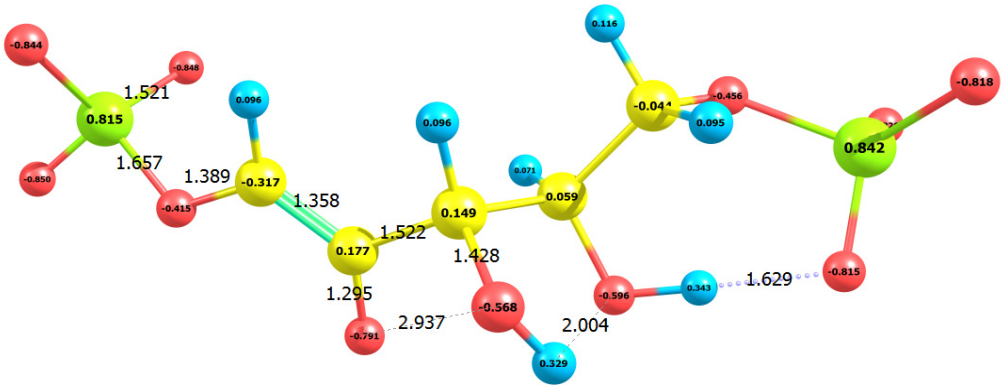

(**a**)

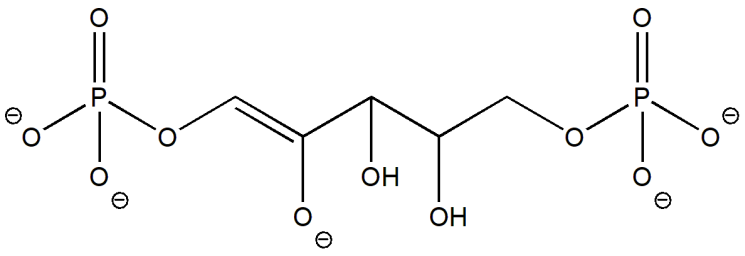

(**b**)

Figure A5. (**a**) The calculated geometric and electronic structure of 1/2-ene(mono/di)olate (1,2-enolate); Q = −5, M = 1, E_0 = −46,424.13 eV, G_0 = −46,421.11 eV. Hessian has negative frequencies: −135.86, −98.86 (cm^{-1}). (**b**) The scheme of (Z)-3,4-dihydroxy-2-oxidopent-1-ene-1,5-diyl diphosphate.

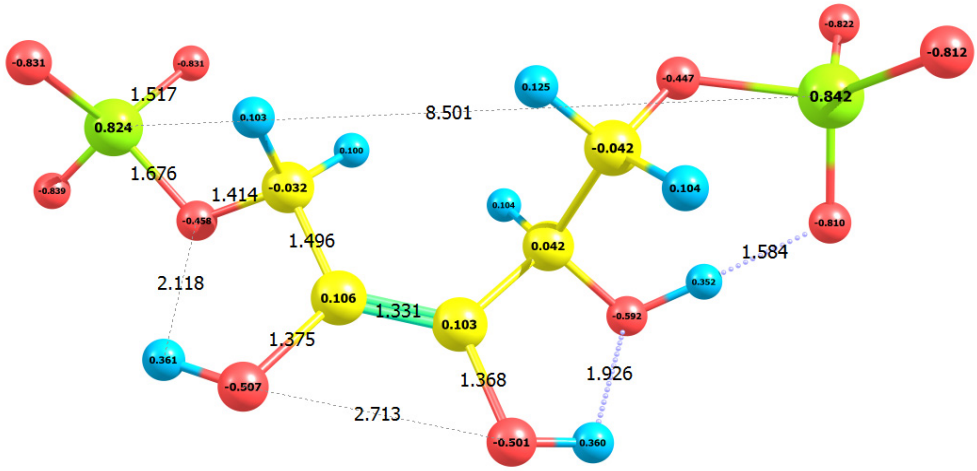

(**a**)

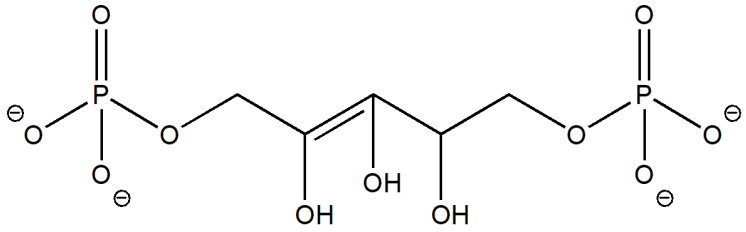

(**b**)

Figure A6. (**a**) The calculated geometric and electronic structure of 1/2-ene(mono/di)ol (2,3-enediol); Q = −4, M = 1, E_0 = −46,437.74 eV, G_0 = −46,434.39 eV. Hessian has negative frequencies: −24.51 (cm^{-1}). (**b**) The scheme of (Z)-2,3,4-trihydroxypent-2-ene-1,5-diyl diphosphate.

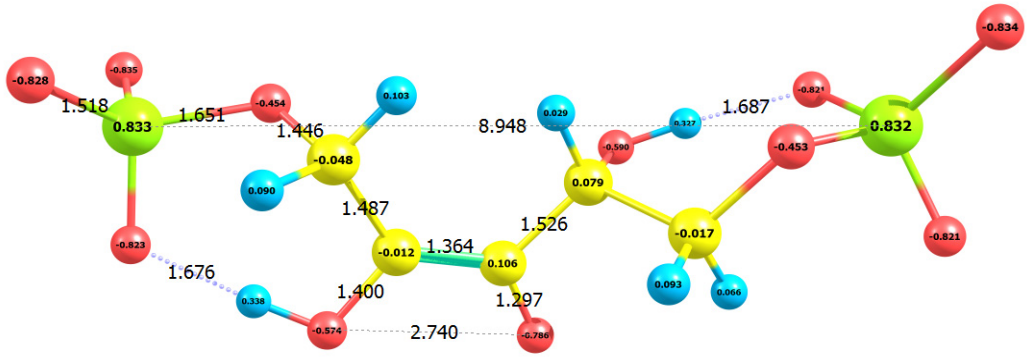

(**a**)

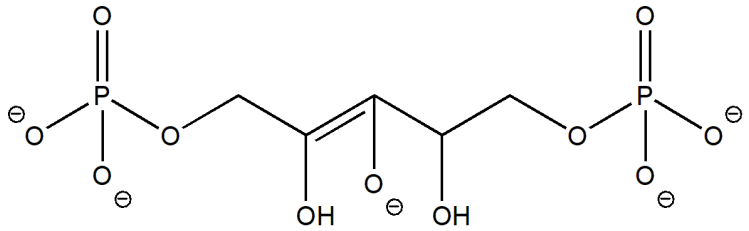

(**b**)

Figure A7. (**a**) The calculated geometric and electronic structure of 1/2-ene(mono/di)olate (2,3-enediolate); Q = −5, M = 1, E_0 = −46,424.27 eV, G_0 = −46,421.25 eV. Hessian has negative frequencies: −28.34 (cm^{-1}). (**b**) The scheme of (Z)-2,4-dihydroxy-3-oxidopent-2-ene-1,5-diyl diphosphate.

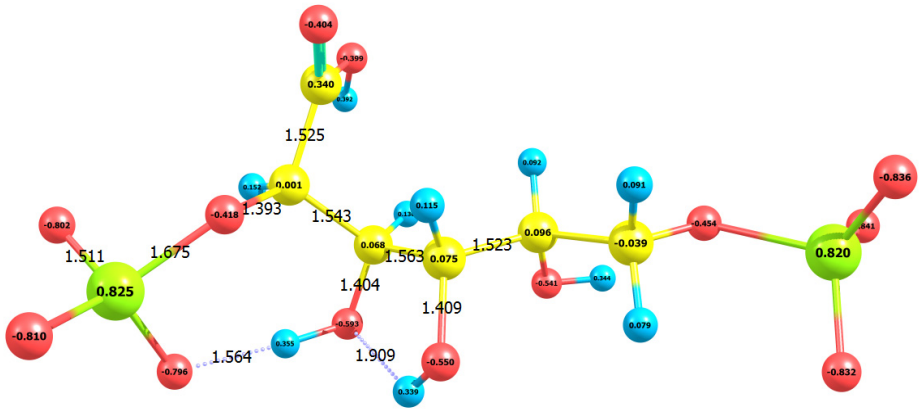

(**a**)

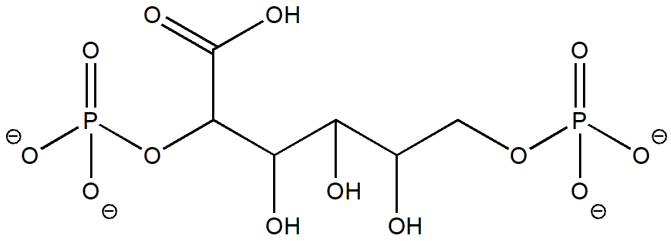

(**b**)

Figure A8. (**a**) The calculated geometric and electronic structure of 2,6-bisphosphate gluconic acid (BPGA); Q = −4, M = 1, E_0 = −51,603.38 eV, G_0 = −51,599.04 eV. Hessian has negative frequencies: −33.21 (cm^{-1}). (**b**) The scheme of 1-carboxy-2,3,4-trihydroxypentane-1,5-diyl diphosphate.

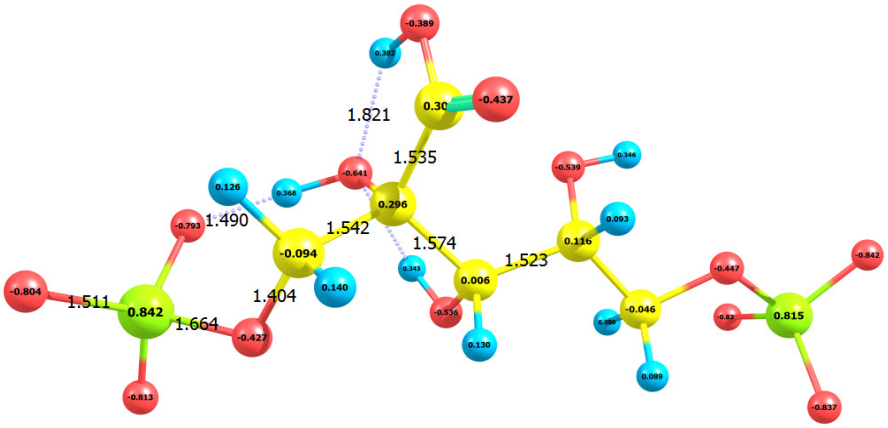

(**a**)

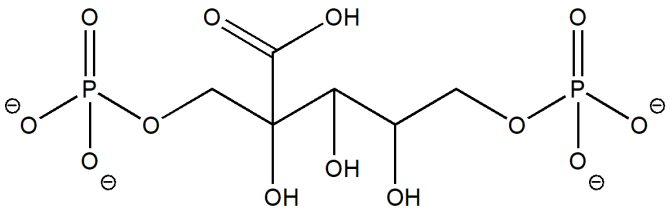

(**b**)

Figure A9. (**a**) The calculated geometric and electronic structure of 2-carboxy-D-arabinitol 1,5-bisphosphate (CABP); Q = −4, M = 1, E_0 = −51,603.53 eV, G_0 = −51,599.18 eV. Hessian has negative frequencies: −82.12, −18.16 (cm^{-1}). (**b**) The scheme of 2-carboxy-2,3,4-trihydroxypentane-1,5-diyl diphosphate.

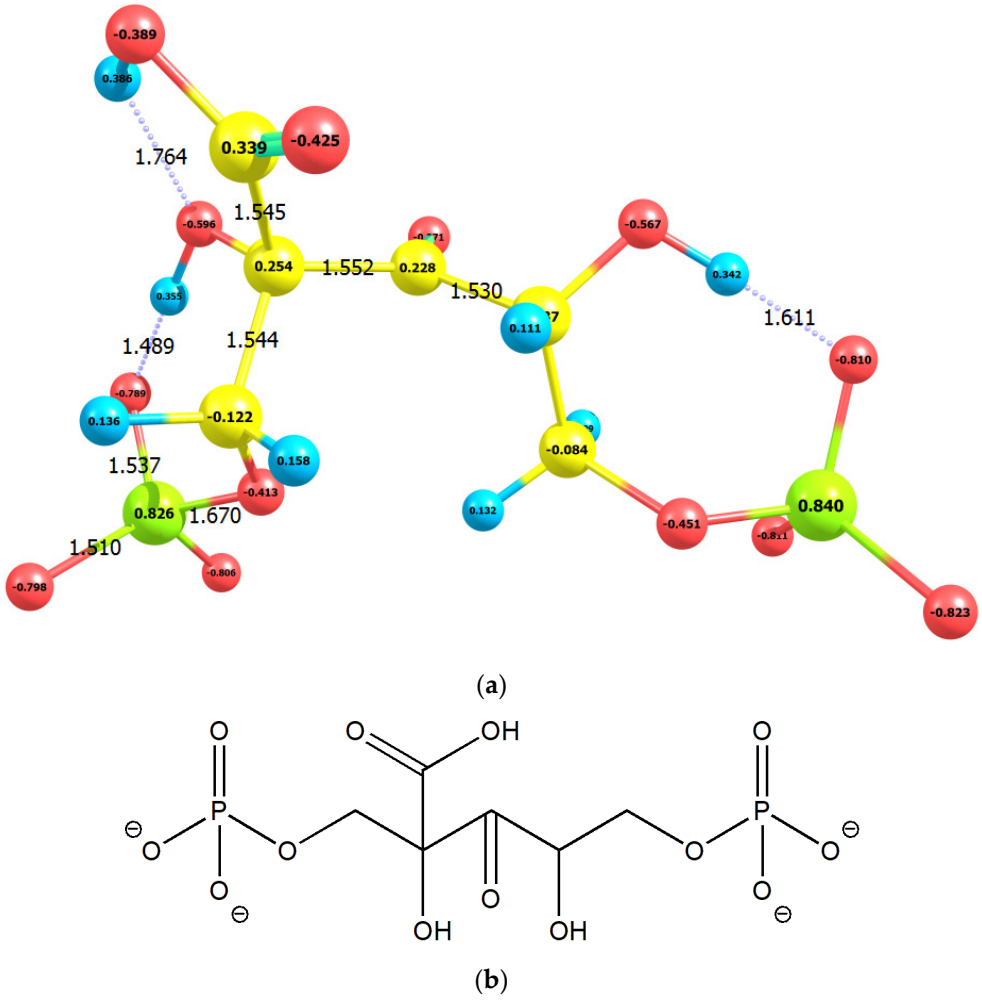

Figure A10. (**a**) The calculated geometric and electronic structure of 3-keto-2-carboxy-D-arabinitol 1,5-bisphosphate (3kCABP); Q = −4, M = 1, E_0 = −51,570.72 eV, G_0 = −51,567.08 eV. Hessian has no negative frequencies. (**b**) The scheme of 2-carboxy-2,4-dihydroxy-3-oxopentane-1,5-diyl diphosphate.

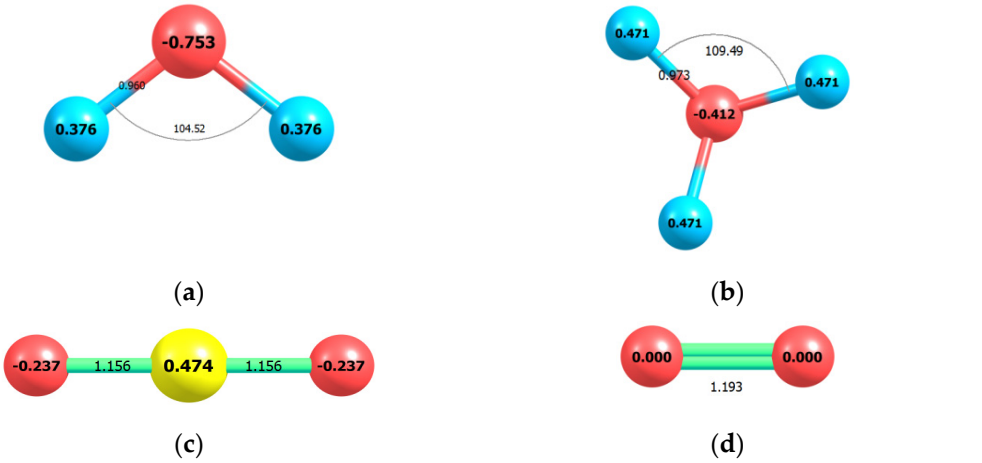

Figure A11. The calculated geometric and electronic structures: (**a**) H_2O, Q = 0, M = 1, E_0 = −2080.34 eV, G_0 = −2080.25 eV; (**b**) H_3O^+, Q = 1, M = 1, E_0 = −2091.54 eV, G_0 = −2091.10 eV; (**c**) CO_2, Q = 0, M = 1, E_0 = −5132.52 eV, G_0 = −5132.76 eV; (**d**) O_2, Q = 0, M = 3, E_0 = −4091.14 eV, G_0 = −4091.58 eV.

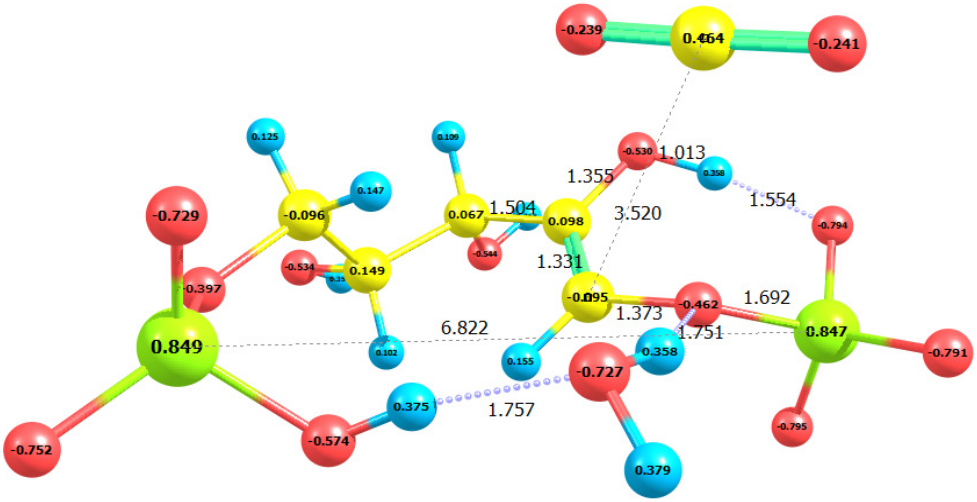

(**a**)

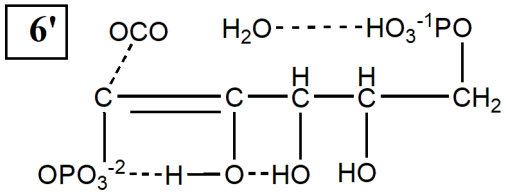

(**b**)

Figure A12. (**a**) The calculated geometric and electronic structures of the initial state of carboxylation in the C1 direction; Q = −3, M = 1, E_0 = −53,664.08 eV, G_0 = −53,659.65 eV. Hessian has no negative frequencies. (**b**) The scheme of state (6′) is pictured in Figure 5b.

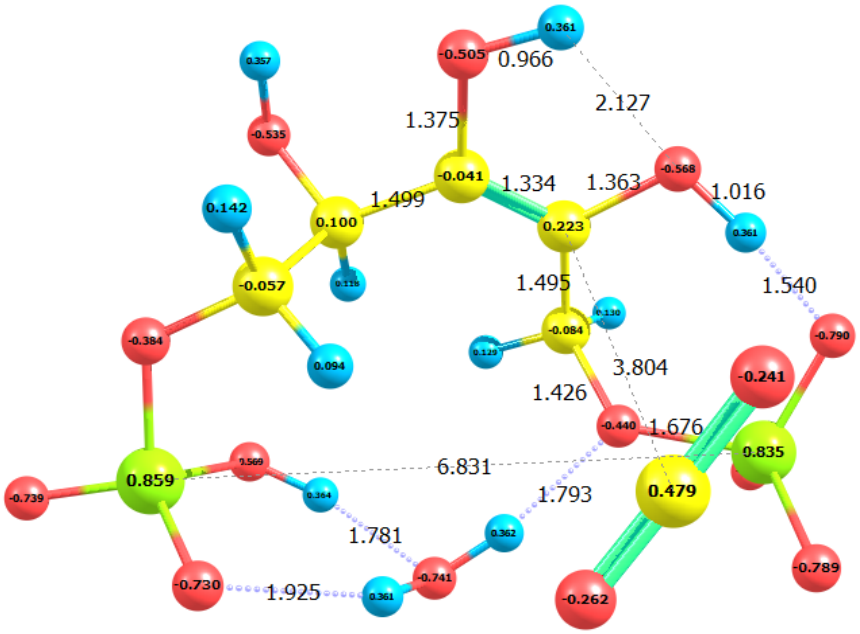

(**a**)

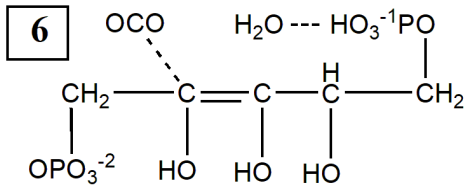

(**b**)

Figure A13. (**a**) The calculated geometric and electronic structure of initial state of carboxylation in C2 direction; Q = −3, M = 1, E_0 = −53,664.37 eV, G_0 = −53,659.83 eV. Hessian has no negative frequencies. (**b**) The scheme of state (6) is pictured in Figure 5a.

References

1. Sage, R.F.; Sage, T.L. C_4 Plants. In *Encyclopedia of Biodiversity*, 2nd ed.; Levin, S.A., Ed.; Academic Press: Pachuca, México, 2013; Volume 2, pp. 361–381.
2. Zhu, X.G.; Long, S.P. Improving Photosynthetic Efficiency for Greater Yield. *Annu. Rev. Plant Biol.* **2010**, *61*, 235–261. [CrossRef] [PubMed]
3. Weber, A.P.M.; Bar-Even, A. Update: Improving the Efficiency of Photosynthetic Carbon Reactions. *Plant Physiol.* **2019**, *179*, 803–812. [CrossRef]
4. Miller, T.E.; Beneyton, T.; Schwander, T.; Diehl, C.; Girault, M.; McLean, R.; Chotel, T.; Claus, P.; Socorro Cortina, N.; Baret, J.-C.; et al. Light-powered CO_2 fixation in a chloroplast mimic with natural and synthetic parts. *Science* **2020**, *368*, 649–654. [CrossRef] [PubMed]
5. Bar-Even, A.; Noor, E.; Lewis, N.E.; Milo, R. Design and analysis of synthetic carbon fixation pathways. *PNAS* **2010**, *107*, 8889–8894. [CrossRef] [PubMed]
6. Sokolov, V.A. On a Possible Way to Increase the Efficiency of Photosynthesis. *Dokl. Biochem. Biophys.* **2020**, *491*, 98–100. [CrossRef]
7. Kannappan, B.; Gready, J.E. Redefinition of Rubisco Carboxylase Reaction Reveals Origin of Water for Hydration and New Roles for Active-Site Residues. *J. Am. Chem. Soc.* **2008**, *130*, 15063–15080. [CrossRef]
8. Götze, J.P.; Saalfrank, P. Quantum chemical modeling of the kinetic isotope effect of the carboxylation step in RuBisCO. *J. Mol. Model.* **2012**, *18*, 1877–1883. [CrossRef] [PubMed]
9. Cummins, P.L.; Gready, J.E. Kohn−Sham Density Functional Calculations Reveal Proton Wires in the Enolization and Carboxylase Reactions Catalyzed by Rubisco. *J. Phys. Chem. B* **2020**, *124*, 3015–3026. [CrossRef] [PubMed]
10. El-Hendawy, M.M.; English, N.J.; Mooney, D.A. Comparative studies for evaluation of CO_2 fixation in the cavity of the Rubisco enzyme using QM, QM/MM and linear-scaling DFT methods. *J. Mol. Model.* **2013**, *19*, 2329–2334. [CrossRef]
11. King, W.A.; Gready, J.E.; Andrews, T.J. Quantum Chemical Analysis of the Enolization of Ribulose Bisphosphate: The First Hurdle in the Fixation of CO_2 by Rubisco. *Biochemistry* **1998**, *37*, 15414–15422. [CrossRef]

12. El-Hendawy, M.M.; Garate, J.-A.; English, N.J.; O'Reilly, S.; Mooney, D.A. Diffusion and interactions of carbon dioxide and oxygen in the vicinity of the active site of Rubisco: Molecular dynamics and quantum chemical studies. *J. Chem. Phys.* **2012**, *137*, 145103. [CrossRef] [PubMed]
13. Cummins, P.L.; Kannappan, B.; Gready, J.E. Revised mechanism of carboxylation of ribulose-1,5-biphosphate by rubisco from large scale quantum chemical calculations. *J. Comput. Chem.* **2018**, *39*, 1656–1665. [CrossRef]
14. Cummins, P.L.; Kannappan, B.; Gready, J.E. Ab Initio Molecular Dynamics Simulation and Energetics of the Ribulose-1,5-biphosphate Carboxylation Reaction Catalyzed by Rubisco: Toward Elucidating the Stereospecific Protonation Mechanism. *J. Phys. Chem. B* **2019**, *123*, 2679–2686. [CrossRef]
15. Chai, J.-D.; Head-Gordon, M. Systematic optimization of long-range corrected hybrid density functional. *J. Chem. Phys.* **2008**, *128*, 084106. [CrossRef] [PubMed]
16. Lin, Y.-S.; Li, G.-D.; Mao, S.-P.; Chai, J.-D. Long-Range Corrected Hybrid Density Functionals with Improved Dispersion Corrections. *J. Chem. Theory Comput.* **2013**, *9*, 263–272. [CrossRef] [PubMed]
17. Grimme, S.; Antony, J.; Ehrlich, S.; Krieg, H. A consistent and accurate ab initio parametrization of density functional dispersion correction (DFT-D) for the 94 elements H-Pu. *J. Chem. Phys.* **2010**, *132*, 154104. [CrossRef] [PubMed]
18. Neese, F.; Wennmohs, F.; Hansen, A.; Becker, U. Efficient, approximate and parallel Hartree–Fock and hybrid DFT calculations. A 'chain-of-spheres' algorithm for the Hartree–Fock exchange. *Chem. Phys.* **2009**, *356*, 98–109. [CrossRef]
19. Weigend, F. Accurate Coulomb-fitting basis sets for H to Rn. *Phys. Chem. Chem. Phys.* **2006**, *8*, 1057. [CrossRef] [PubMed]
20. Weigend, F.; Ahlrichs, R. Balanced basis sets of split valence, triple zeta valence and quadruple zeta valence quality for H to Rn: Design and assessment of accuracy. *Phys. Chem. Chem. Phys.* **2005**, *7*, 3297. [CrossRef] [PubMed]
21. Barone, V.; Cossi, M.; Tomasi, J. A New Definition of Cavities for the Computation of Solvation Free Energies by the Polarizable Continuum Model. *J. Chem. Phys.* **1997**, *107*, 3210. [CrossRef]
22. Cossi, M.; Scalmani, G.; Rega, N.; Barone, V. New Developments in the Polarizable Continuum Model for Quantum Mechanical and Classical Calculations on Molecules in Solution. *J. Chem. Phys.* **2002**, *117*, 43. [CrossRef]
23. Tomasi, J.; Mennucci, B.; Cammi, R. Quantum Mechanical Continuum Solvation Models. *Chem. Rev.* **2005**, *105*, 2999–3094. [CrossRef] [PubMed]
24. Neese, F. Software update: The ORCA program system, version 4.0. *Wiley Interdiscip. Rev. Comput. Mol. Sci.* **2018**, *8*, e1327. [CrossRef]
25. Chemcraft-Graphical Software for Visualization of Quantum Chemistry Computations. Available online: https://www.chemcraftprog.com (accessed on 1 January 2021).